

# A Column-Row-Parallel Ultrasound Imaging Architecture for 3D Plane-wave Imaging and Tx 2nd-Order Harmonic Distortion (HD2) Reduction

Kailiang Chen\*, Byung Chul Lee<sup>†</sup>, Kai Thomenius\*, Butrus T. Khuri-Yakub<sup>†</sup>, Hae-Seung Lee\*, Charles G. Sodini\*

\*Department of Electrical Engineering and Computer Science

Massachusetts Institute of Technology

Cambridge, MA 02139, U.S.A.

Email: chenkl@alum.mit.edu

<sup>†</sup>Department of Electrical Engineering

Stanford University

Stanford, CA 94305, U.S.A.

**Abstract**—We propose a Column-Row-Parallel (CRP) architecture for integrated and low-power 3D medical ultrasound imaging applications. CRP offers linear-scaling interconnection, acquisition and programming time, while supporting rich functionality and fault-tolerance against possible transducer element defects. A 16x16 CMUT-ASIC CRP imaging system is fabricated and assembled to demonstrate the highly versatile architecture. 3D plane-wave coherent compounding on CRP facilitates fast frame rate (62.5 volume/s), high quality 3D ultrasonic imaging. An interleaved checker board pattern with I&Q excitations is also demonstrated on CRP for tissue harmonic imaging, reducing CMUT 2nd harmonic distortion (HD2) emission by over 20dB.

## I. INTRODUCTION

A 3D medical ultrasonic imaging system provides a volumetric view of human tissue or organs that is comprehensive for medical interpretation. However, interconnection and power dissipation issues become severe bottlenecks for hardware implementation of such a system in real-time, due to the large channel count associated with the 2D ( $N \times N$ ) transducer and the corresponding array of front-end transceiver electronics. CMUT in conjunction with the integrated circuit (ASIC) technology are promising to solve this hardware integration problem, if an efficient system architecture is in place.

To interface to the 2D transducer array, a fully-parallel circuit architecture requires  $N^2$  independent transceivers and I/Os, which is difficult to scale up economically as the array size grows larger. On the other extreme, a single-channel transceiver that serially sweeps the  $N^2$  elements slows down the frame rate excessively. In between the two extremes, sub-array architectures such as diagonal or cross [1], and sparse arrays [2] have been proposed, but they suffer from weakened emitted acoustic energy and elevated side-lobe levels. In [3], 3x3 or 5x5 sub-arrays with programmable focal points manage to maintain good image quality, but the use of analog delay lines leads to large power and silicon area. Similarly, a column-parallel (row-by-row) architecture [4] reduces active channel count from  $N^2$  to  $N$ , but its elevation beam-formation still

relies on analog delay lines. To cover both azimuth and elevation beam-formation (BF) without using analog delay lines, column-row addressing schemes have been implemented on transducer designs [5]–[7]. However, because the transducer array is hard-wired to be addressed only by rows or columns, it imposes heavy restrictions for the supporting beamforming algorithm. In contrast, this paper proposes a Column-Row-Parallel (CRP) architecture at the circuit-level instead of transducer-level. Various sub-array apertures are supported under the highly programmable element addressing scheme. It achieves 3D beam-formation with much more flexibility and better tradeoff between complexity and speed.

## II. THE COLUMN-ROW-PARALLEL ARCHITECTURE

Fig. 1(a) shows the proposed CRP architecture. Its transistor-level ASIC implementation in 0.18 $\mu$ m HV CMOS (die photo in Fig. 1(b)) has been presented in [8], [9]; this paper focuses on its functional description and imaging applications. A 2D CMUT (16x16 SOI CMUTs are used in this work) is DC biased from the common top membrane with a shared off-chip RC network. Each CMUT element's bottom pad is connected to its corresponding ASIC front-end channel, which is composed of a transmitter (Tx) pulser, a receiver (Rx) low noise amplifier (LNA), and a receiver high voltage (HV) protection switch; their silicon area is element-matched to the CMUT pitch (250 $\mu$ m  $\times$  250 $\mu$ m in this work) for compact flip-chip bonding assembly through a PCB interposer (Fig. 1(c)). Meanwhile, the Tx pulser drivers and Rx line buffer amplifiers are placed at the ASIC perimeter to interface to the front-end array. There are  $N$  copies of Tx drivers and Rx buffers at the column side and another  $N$  copies at the row side, reducing the ASIC I/Os down to  $N^1$ .

The CRP array operates either in column-parallel or row-parallel mode, controlled by a combination of row select,

<sup>1</sup>Column and row side I/Os are further multiplexed to combine from  $2N$  to  $N$ , not shown in Fig. 1(a) but discussed in [8], [10].

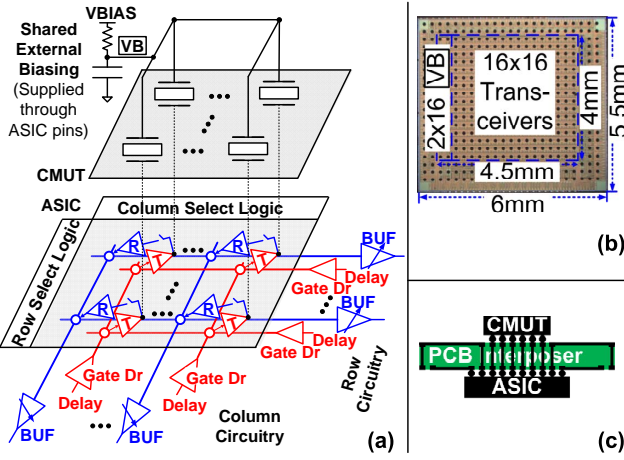


Fig. 1. (a) Column-Row-Parallel architecture block diagram; (b) die photo of the CRP ASIC fabricated in  $0.18\mu\text{m}$  HV CMOS; (c) CMUT and ASIC chips are element-matched and flip-chip bonded through a PCB interposer.

column select and per-element enabling logic. In column-parallel mode, the column circuitry is active while the row select logic determines which elements are parallelized along each column. For example, in Fig. 2(a), two Tx elements are activated in parallel for each column, driven by a shared column driver. Tx azimuth beam-formation is realized by applying relative delays to 16 column drivers. Similarly, Fig. 2(b) shows an Rx aperture in row-parallel mode; the row circuitry and the column select logic are active. Five active Rx channels along the same row are in parallel. Their signals are averaged and output by the row buffer. Rx elevation beam-formation is implemented with delay and sum across the 16 row signals after digitization. Note that Tx and Rx apertures are independent; each can be put in either column- or row-parallel mode. The number of active rows or columns is also programmable. In addition to row-by-row or column-by-column operations, more complex aperture patterns are possible with the use of per-element enable bits in each front-end channel. The intersection of selected rows / columns and asserted individual channels defines the active aperture. Fig. 2(c-f) show examples of Tx checker board, Rx diagonal, and annular ring apertures, respectively.

The CRP architecture is both scalable and flexible. First, the row-by-row or column-by-column operations reduce complexity of interconnection and data acquisition down to  $N$  for a  $N^2$ -channel system. The columns or rows are reprogrammable for flexible 3D beam-formation; the programming time also scales with  $N$  ( $0.16\mu\text{s}$  by a  $100\text{MHz}$  clock). Second, per-element enable bits are programmed by snake-chained shift-registers (SRs) through the array, which offer fine granularity for application-specific patterns, making CRP compatible with existing BF schemes [1], [2], [4]–[7], while enabling new ones as will be discussed next. Third, each control set (column, row, per-element) has two multiplexed SR banks to allow operation based on one bank while reprogramming the other; or alternating two pre-programmed banks for fast imaging aperture switching. Lastly, the per-element enable bits introduce fault-tolerance against defective shorting CMUT elements in the

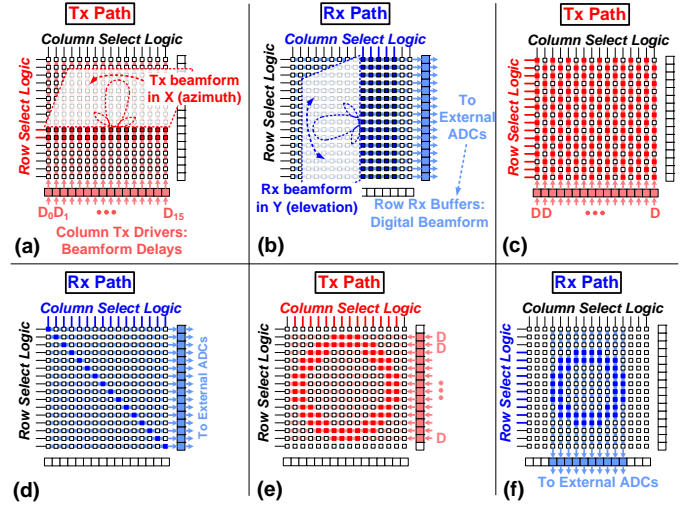


Fig. 2. Example apertures in CRP architecture: (a) a Tx aperture in column-parallel mode with azimuth beam-formation; (b) an Rx aperture in row-parallel mode with elevation beam-formation; (c) a checker board Tx aperture for tissue harmonic imaging; (d) a diagonal Rx aperture; (e-f) annular ring Tx and Rx apertures for forward-looking ultrasonic imaging applications.

array, which is important in boosting assembly yield and test speed as CMUTs scale to higher spatial resolution<sup>2</sup>.

### III. 3D PLANE-WAVE COHERENT COMPOUNDING ON CRP

Because of the parallelism along both column and row directions, the CRP architecture can extend the 2D plane-wave operation [11] into 3D, and perform fast frame rate imaging with 3D plane-wave coherent compounding (PWCC3D).

Fig. 3 shows the  $16 \times 16$  CRP configuration for PWCC3D. All array elements are programmed to be active during transmit to form plane-waves steered at different angles. In Fig. 3(a), the Tx aperture is configured in column-parallel mode; each column contains 16 active elements in parallel and is driven by a Tx pulser driver at the column side. The 16 column drivers are programmed to supply a linear delay profile with respect to each other, thus generating plane-wave wavefronts tilted at different angles ( $\alpha_1 \dots \alpha_p$ ) along X direction, implementing the azimuth plane-wave steering. Similarly, to achieve steering along the elevation (Y) direction, as shown in Fig. 3(b), the Tx aperture is arranged in row-parallel mode, and 16 elements along the same row are driven by the shared Tx pulser driver at the row side. The 16 row drivers control the plane-wave tile angle along Y ( $\beta_1 \dots \beta_p$ ). To collect ultrasound echo signals reflected at a given Tx angle, Rx aperture is activated row-by-row in column-parallel mode as shown in Fig. 3(c). In each reception, 16 analog waveforms are acquired from the activated elements, and the full 256 echo waveforms are acquired after 16 Tx-Rx repetitions.

Fig. 3(d) illustrates the PWCC3D processing flow after Rx data for all Tx angles are collected. Given a Tx plane-wave angle along azimuth  $\alpha$ , or elevation  $\beta$ , the delay-and-sum beamforming delay values represent the time-of-flight<sup>3</sup>

<sup>2</sup>The fault-tolerance provided by CRP is critical for successful CMUT-ASIC integration in our work, it is described in detail in [8].

<sup>3</sup> $c$  is sound speed.

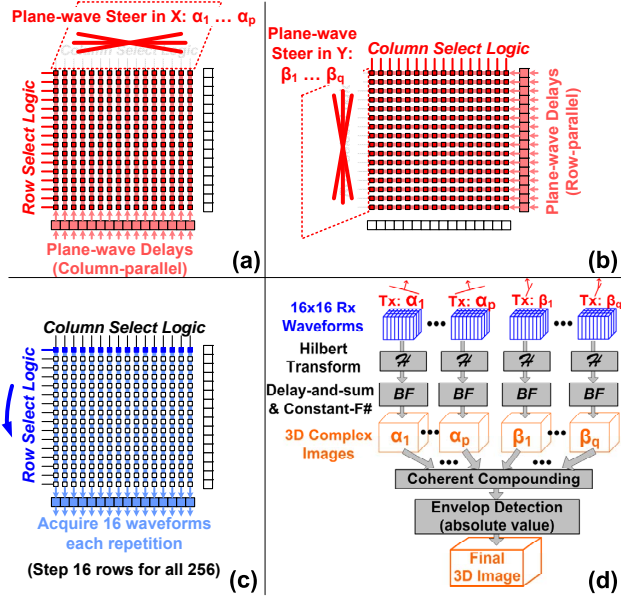


Fig. 3. PWCC3D implemented on CRP: (a) Tx beam-steering along azimuth (X) direction using column-parallel mode; (b) Tx beam-steering along elevation (Y) direction using row-parallel mode; (c) A complete set of Rx signals is acquired by sweeping through 16 rows with 16 Tx-Rx repetitions; (d) 3D beam-forming signal processing flow for PWCC3D on CRP.

from center of the transducer array  $(0, 0, 0)$  to an image voxel at  $(x, y, z)$  as in (1); then back to the receiving element at  $(x_1, y_1, 0)$  as in (2). 3D images in complex value are formed for every Tx angle. Coherent compounding is then carried out across all angles, by adding voxel values in complex domain. The final compounded 3D image is obtained by taking the magnitude of the complex value voxels (envelope detection).

$$\begin{cases} \tau_{TX\_azimuth}(\alpha, x, y, z) = (z \cdot \cos \alpha + x \cdot \sin \alpha) / c, \\ \tau_{TX\_elevation}(\beta, x, y, z) = (z \cdot \cos \beta + y \cdot \sin \beta) / c. \end{cases} \quad (1)$$

$$\tau_{RX}(x_1, y_1, x, y, z) = \sqrt{z^2 + (x - x_1)^2 + (y - y_1)^2} / c. \quad (2)$$

This CRP PWCC3D processing scheme allows a software beamformer that is low-power and flexible with speed and quality tradeoff. Data acquisition is only performed once, while beam-formation on each voxel is independent and utilizes the same set of data. One can perform coarse imaging over a large space; and a higher definition second-pass over a smaller space, after spotting features of interest.

The volumetric images of a metal ring phantom are acquired by the 16x16 CRP CMUT-ASIC front-end assembly. The ring is placed horizontally above the transducer surface at a distance of 7.5mm. The Tx pulsation is 2 bursts of 8.33MHz pulses; a constant F-number of 1.75, and rectangular windows are used for Tx and Rx apodization. Single-angle images are compared against ones compounded with 5 X-angles and 5 Y-angles at  $(-6.7^\circ, -3.3^\circ, 0^\circ, 3.3^\circ, 6.7^\circ)$ , as in Fig. 4(a-b). The 10-angle compounded cross-sectional image shows higher contrast and lower side-lobes. Fig. 4(c-d) quantify that the side-lobes in the center of the ring is improved by 6dB with

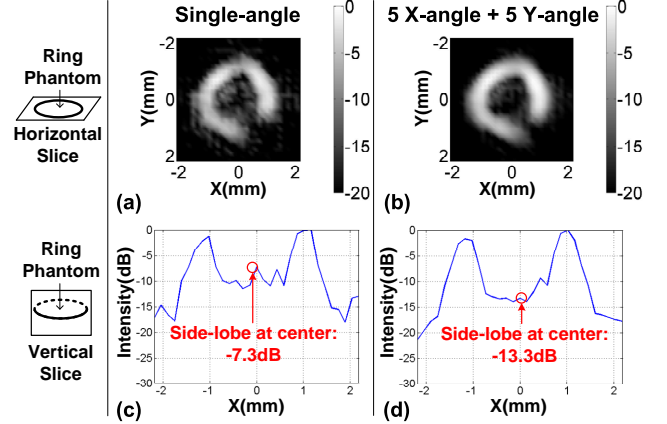


Fig. 4. Measured cross-sectional images of a ring phantom: (a) horizontal slice image from single-angle Tx plane-wave; (b) horizontal slice from compounded plane-waves; (c) lateral resolution plot of ring image from (a); (d) lateral resolution plot from (b) with suppressed side-lobes.

10-angle coherent compounding (from -7.3dB to -13.3dB). Similarly, experimental images of a wire phantom (not shown) further demonstrates a 46% improvement of -10dB lateral resolution (from 1.32mm to 0.71mm) with 10-angle compounding. A 10kHz pulse repetition frequency (PRF) is used for the 10-angle compounding scheme in our experiments, leading to a frame rate of 62.5 volume/s. The frame rate decreases linearly with increase in the array size, or number of plane-wave angles, to trade for better image quality.

#### IV. TX HD2 REDUCTION USING CRP

Compared to traditional PZT transducers, it is difficult to use CMUT for tissue harmonic imaging because of its nonlinear electrostatic actuation mechanism, where excessive HD2 is generated during transmit. Previous solutions include: predistortion [12] and bias modulation [13], which rely on parameter fine tuning according to CMUT transfer function. Second harmonic inversion [14] must use two consecutive  $I$  and  $Q$  pulses for HD2 cancellation synthetically.

In this work, the CRP architecture facilitates an interleaved checker board aperture for second harmonic inversion in one Tx shot. As in Fig. 5, two banks of Tx per-element enable bits, Bank1 in red and Bank2 in yellow, are pre-programmed into interleaved checker board patterns. By quickly switching active Tx apertures between the two banks, the column pulser drivers are able to drive Bank1 elements with  $I(t)$  pulses and Bank2 with  $Q(t)$  simultaneously, where  $Q(t)$  is time-delayed by a quarter pulse cycle with respect to  $I(t)$ . The pulse signals go through a nonlinear quadratic transfer function into the emitted acoustic pressure. It can be proved [10] that for any arbitrary pulse shape, the fundamental component of acoustic pressure generated by  $I(t)$  and  $Q(t)$  are out of phase by  $\pi/2$ , leading to a 3dB intensity reduction compared to a full-array excitation; meanwhile, the 2nd harmonic component<sup>4</sup>

<sup>4</sup>It is interesting to mention that not only second harmonic, but  $6^{th}$ ,  $10^{th}$ ,  $14^{th}$ , etc.  $((2 + 4 \cdot k)^{th}, k = 0, 1, 2, \dots)$  are also out of phase by integer multiples of  $\pi$ . Reductions in  $6^{th}$  and  $10^{th}$  components are observed in measurement, while higher harmonics are too weak to see.

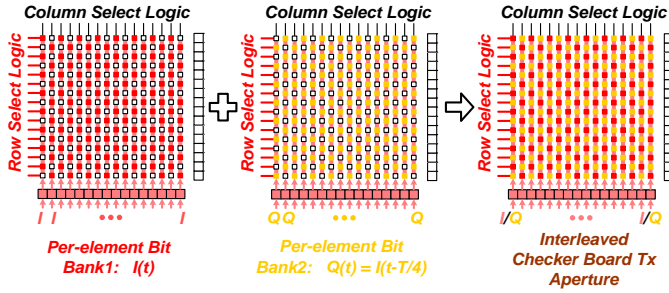


Fig. 5. Implementation of checker board Tx aperture on the proposed architecture.

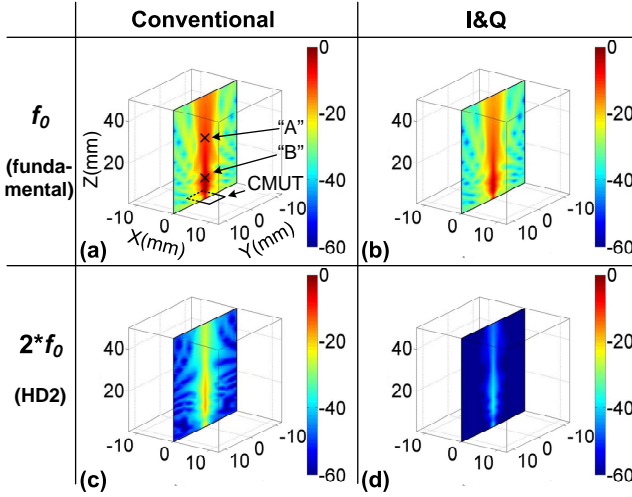


Fig. 6. Simulation comparison of spatial acoustic pressure intensity between the conventional and I&Q methods: (a) fundamental, conventional; (b) fundamental, I&Q; (c) HD2, conventional; (d) HD2, I&Q.

are out of phase by  $\pi$  and cancel each other. Furthermore, because a general 2nd-order distortion model is assumed, this method applies not only to CMUT, but also other sources of nonlinearity - for example, HD2 introduced from pulse rise / fall time asymmetry due to circuit mismatches. Lastly, the interleaved checker board patterns require that the element pitch be smaller or approximately equal to the ultrasound wavelength, so that the grating lobes are kept at minimum and the HD2 cancellation in space is close to perfect.

Both Field II [15] simulation and measurement are carried out to verify the theory. Various configurations are used to show that I&Q method is a general and broadband technique: pulse shapes (2-/3-level), number of bursts (2-20), frequencies (2.1/2.8/4.2MHz), pulse amplitudes (10/20/30Vpp), and CMUT bias voltages (20/30/40V) are varied. Fig. 6(a-b) compare the simulated fundamental component of the emitted pressure field, in which the conventional method produces a field with 3dB higher intensity than I&Q. Fig. 6(c-d) compare the simulated HD2 field, revealing a large HD2 suppression from I&Q. The measured normalized field intensity at the same spatial locations as in simulation are summarized in Table I, confirming that the I&Q method has 3dB less fundamental intensity but over 20dB HD2 performance improvement.

TABLE I  
SIMULATED AND MEASURED NORMALIZED ACOUSTIC FIELD PRESSURE, COMPARING CONVENTIONAL V.S. I&Q METHOD.

Simulation	HD2 Reduction	Fundamental Loss
“A” (0, 0, 30.3)mm	-19.7dB	-3.0dB (the whole space)
“B” (0, 0, 10.2)mm	-19.7dB	
Measurement	HD2 Reduction	Fundamental Loss
“A” (0, 0, 30.3)mm	-21.7dB	-3.4dB
“B” (0, 0, 10.2)mm	-22.1dB	-3.2dB

## V. CONCLUSION

In summary, this paper presents a Column-Row-Parallel architecture for low-power, scalable, and fault-tolerant 3D medical ultrasound hardware, offering linear scaling of interconnection, acquisition and programming time. Besides supporting many existing beam-formation schemes, the experimental 16x16 CMUT-ASIC CRP system demonstrates 3D plane-wave coherent compounding, achieving 62.5 volume/s frame rate with improved image contrast; and an I&Q excitation scheme that reduces Tx HD2 by over 20dB, applicable to nonlinear transducers and circuits with arbitrary pulse shapes.

## ACKNOWLEDGMENT

This work was partially funded by the C2S2 Focus Center, one of six research centers funded under the Focus Center Research Program (FCRP), a Semiconductor Research Corporation entity; and Texas Instruments. We thank TSMC for ASIC fabrication and MIT Lincoln Lab for flip-chip assembly.

## REFERENCES

- [1] S. Smith *et al.*, “High-speed ultrasound volumetric imaging system. i. transducer design and beam steering,” *IEEE UFFC*, 1991.
- [2] M. Karaman *et al.*, “Minimally redundant 2-d array designs for 3-d medical ultrasound imaging,” *Medical Imaging, IEEE Trans. on*, 2009.
- [3] B. Savord and R. Solomon, “Fully sampled matrix transducer for real time 3d ultrasonic imaging,” in *IEEE Ultrasonics Symposium*, 2003.
- [4] B.-H. Kim *et al.*, “Hybrid volume beamforming for 3-d ultrasound imaging using 2-d cmut arrays,” in *IEEE Ultrasonics Symposium*, 2012.
- [5] C. H. Seo and J. Yen, “A 256 x 256 2-d array transducer with row-column addressing for 3-d rectilinear imaging,” *IEEE UFFC*, 2009.
- [6] M. Rasmussen *et al.*, “3-d ultrasound imaging performance of a row-column addressed 2-d array transducer: A measurement study,” *IUS’13*.
- [7] A. Savoia *et al.*, “Crisscross 2d cmut array: Beamforming strategy and synthetic 3d imaging results,” in *IEEE Ultrasonics Symposium*, 2007.
- [8] K. Chen, H.-S. Lee, and C. Sodini, “A column-row-parallel asic architecture for 3d wearable / portable medical ultrasonic imaging,” in *IEEE VLSI Symposia*, 2014.
- [9] K. Chen, H.-S. Lee, A. Chandrakasan, and C. Sodini, “Ultrasonic imaging transceiver design for cmut: A three-level 30-vpp pulse-shaping pulser with improved efficiency and a noise-optimized receiver,” *Solid-State Circuits, IEEE Journal of*, vol. 48, no. 11, pp. 2734–2745, 2013.
- [10] K. Chen, “A column-row-parallel asic architecture for 3d wearable / portable medical ultrasonic imaging,” Ph.D. dissertation, MIT, 2014.
- [11] G. Montaldo *et al.*, “Coherent plane-wave compounding for very high frame rate ultrasonography and transient elastography,” *IEEE UFFC*, 09.
- [12] S. Satir *et al.*, “Harmonic reduction in capacitive micromachined ultrasonic transducers by gap feedback linearization,” *IEEE UFFC*, 2012.
- [13] A. Novell *et al.*, “Evaluation of bias voltage modulation sequence for nonlinear contrast agent imaging using a capacitive micromachined ultrasonic transducer array,” *Physics in medicine and biology*, 2014.
- [14] M. Pasovic *et al.*, “Second harmonic inversion for ultrasound contrast harmonic imaging,” *Physics in Medicine and Biology*, 2011.
- [15] J. Jensen, “Field: A program for simulating ultrasound systems,” in *NordicBaltic Conference on Biomedical Imaging*, 1996.